

See discussions, stats, and author profiles for this publication at: <https://www.researchgate.net/publication/260499548>

Arrangement of Block Copolymer Microdomains Confined inside Hemispherical Cavities

ARTICLE *in* MACROMOLECULES · JULY 2013

Impact Factor: 5.8 · DOI: 10.1021/ma4009324

CITATIONS

6

READS

39

5 AUTHORS, INCLUDING:



Hiroshi Jinnai

Tohoku University

234 PUBLICATIONS 4,234 CITATIONS

SEE PROFILE

Arrangement of Block Copolymer Microdomains Confined inside Hemispherical Cavities

Dusik Bae,[†] Gumhye Jeon,[†] Hiroshi Jinnai,[‡] June Huh,^{*,§} and Jin Kon Kim^{*,†}

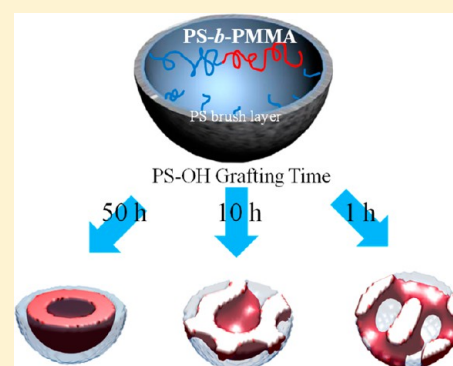
[†]National Creative Research Center for Block Copolymer Self-Assembly, Department of Chemical Engineering, Pohang University of Science and Technology, Kyungbuk 790-784, Korea

[‡]Department of Materials Chemistry and Engineering, Japan Science and Technology Agency, ERATO, Takahara Soft Interfaces Project, Kyushu University, 744 Motooka, Nishi-ku, Fukuoka 819-0395, Japan

[§]Department of Materials Science and Engineering, Yonsei University, 134 Shinchon-dong, Seodaemun-gu, Seoul 120-749, Korea

S Supporting Information

ABSTRACT: We investigated, via scanning and transmission electron microscopy, the arrangement of the microdomains of symmetric polystyrene-*block*-poly(methyl methacrylate) copolymer (PS-*b*-PMMA) confined in hemispherical cavities. The hemispherical cavities were prepared by using anodic aluminum oxide (AAO) template, where the inner surface of the cavities was modified by thin brush layers of PS, PMMA, and PS-*ran*-PMMA copolymer. When the inner surface of the cavity is strongly selective to PS chains, concentric rings consisting of PS and PMMA microdomains are formed, replicating the confined geometry of hemisphere. However, as the selectivity of a brush to PS chains becomes weaker, various interesting morphologies are formed that have not been reported in the literature. The experimentally observed microdomain arrangement confined inside the hemispherical cavities was compared with the simulation results based on the dynamic Metropolis Monte Carlo method.



1. INTRODUCTION

Block copolymers (BCPs), comprised of two or more chemically different polymeric blocks covalently linked together, have gained much interest owing to their ability to self-assemble into various nanoscopically ordered structures in molten state, such as lamellae, gyroids, cylinders, and spheres.¹ These spatially periodic nanostructures can be used in various potential applications such as high density data storage media, lithographic patterning, optical materials, membranes, and templates for harvesting metal or inorganic materials.^{2–11} Also, one can create novel microdomain morphologies and defect-free long-range ordering of the microdomains when the block copolymer self-assembly is combined with electrospinning, dewetting, geometrical confinement (or graphoepitaxy), and chemical patterns, which has been referred to the directed self-assembly (DSA).^{12–15}

Nanoscale confinement of BCPs offers a promising means to provide defect-free microdomain structures or to manipulate nontraditional morphologies completely different from their bulk morphologies. Numerous research groups have investigated the confinement effect on the BCP morphology experimentally or theoretically.^{16–22} Confinement geometry can be classified into 1-, 2-, and 3-dimensions. 1-D confinement, where the spatial restriction is imposed on only one direction, is achieved simply by confining BCPs between two planar plates, which perturbs not only nonplanar but also planar bulk morphologies. For instance, 1-D confinement alters the domain spacing of lamellar-forming BCP when the plate

separation distance (L) is incommensurate with the lamellar domain spacing in bulk (L_0).²³ 2-D confinement has generally been obtained by confining BCPs into cylindrical nanoporous templates, for instance, anodic aluminum oxide (AAO) membrane. Depending on the diameter of the membrane pore (D) relative to the microdomain spacing of the block copolymer in bulk, various morphologies have been reported, such as concentric rings and helical structures.¹⁵ BCPs under 3-D confinement where they are in spherical pores (or cavities) exhibit onion-like and stacked lamellae, screw, janus, tennis ball, and helix.^{17,24–29}

Trenches in nanosized scale, made by narrow excavation below a supporting surface, have been widely used for guiding or positioning self-assembled patterns of BCPs.³⁰ Under this type of confinement, BCPs are bound not only to the inner surface of the trench but also to the upper medium such as air or solvent vapor, which provide options for directing self-assembly of BCPs toward more desirable nanopatterns. A typical example is that BCPs are confined in a line trench where the orientational and translational orders of BCP microdomain patterns can be greatly enhanced by the sidewall of the line trench.³¹

While most DSA works have concentrated on pattern organization using line trench, very few studies have been done

Received: May 4, 2013

Revised: June 7, 2013

Published: June 19, 2013

for the BCP morphologies confined in other type of geometries such as dimples. An array of hemispherical cavities, which can be fabricated by a proper control of anodization of aluminum, could be used for developing functional materials such as sensors when they are combined with BCP self-assembly.³² In particular, a high density array of the concentric silver nanorings, which show high signal intensity for SERS due to the interference between nanorings, could be readily fabricated by using BCP self-assembly confined in the hemispherical cavities.³⁰ Yu et al.³³ investigated the morphologies of cylinder-forming asymmetric BCP confined in a dimple. They obtained various confined morphologies such as spheres, rings, or the combination of these two. But, the confined morphology of lamellae-forming symmetric BCPs in a dimple has not been investigated yet.

In this study, we investigate the confined morphology of lamellar-forming PS-*b*-PMMA inside the hemispherical cavities. The cavities were prepared by AAO template, and the inner surface of the cavity was modified by anchoring three different polymer brushes (PS, PMMA, and PS-*ran*-PMMA) to the AAO wall, while the top surface of cavity (bound to the air medium) is kept the same, which allowed us to systematically investigate the effect of surface selectivity and the degree of confinement on the arrangement of BCP microdomains. Concentric lamellar layers replicating the boundary of spherical cavity are formed when the inner surface is strongly selective to the one of block, whereas complex layered structures are observed when the surface is neutral to PS and PMMA chains. However, when the inner surface is weakly selective to PS chains, we found various types of the layer modulations such as interface undulation or layer perforations. These experimental results are compared with the simulation results based on the dynamic Metropolis Monte Carlo method.³⁴

2. EXPERIMENT AND SIMULATION

Materials and Sample Preparation. Three different symmetric PS-*b*-PMMA, hydroxyl end-functionalized PS (PS-OH with number-average molecular weight (M_n) = 21 000 g mol⁻¹ (lot no. P9022) and PMMA (PMMA-OH with M_n = 35 000 g mol⁻¹ (lot no. P1719) homopolymers, and hydroxyl end-functionalized PS-*ran*-PMMA (PS-*ran*-PMMA-OH with M_n = 7000 g mol⁻¹ and volume fraction of PS = 57%; lot no. P6469A) were purchased from Polymer Source Inc. and used as received. The molecular characteristics of PS-*b*-PMMA are given in Table 1. The lamellar microdomain spacing (L_0) of three PS-*b*-PMMA was measured by synchrotron small-angle X-ray scattering at the 4C1 beamline of Pohang Accelerator Laboratory with an X-ray radiation source of λ = 0.1608 nm, and a 2-D CCD camera (Princeton Instruments, SCX-TE/CCD-1242) was used to collect the scattered X-rays.³⁵ The sample thickness and the exposure time were 1.0 mm and 100 s, respectively.

Table 1. Molecular Characteristics of PS-*b*-PMMA Employed in This Study

polymer (lot no.)	$M_{n,PS}$ ($\times 10^3$ g mol ⁻¹)	$M_{n,PMMA}$ ($\times 10^3$ g mol ⁻¹)	PDI ^a	L_0 (nm)	f_{PS} ^b
SML-51 (P4961)	25	26	1.06	32.9	0.52
SML-98 (P2355)	50	48	1.13	47.3	0.54
SML-320 (P5543)	160	160	1.09	100	0.53

^aPolydispersity index. ^bVolume fraction of the PS block in PS-*b*-PMMA.

AAO template was prepared by well-established two-step anodization.³² First anodization was performed in 0.1 M phosphoric acid aqueous solution at 0 °C under an applied potential of 195 V to obtain the perfect hexagonal pore arrangement over a large area. The pore size and center-to-center distance between two neighboring pores in this AAO membrane are 100 and 500 nm, respectively. After irregular pores in the AAO were removed, a second anodization was performed at 0 °C and 195 V for 15 s. Finally, the pore diameter was controlled by adjusting pore-widening time in 0.1 M H₃PO₄ aqueous solution at 30 °C (the details are given in section 1 of the Supporting Information).

Figure 1 shows the high density array of hemispherical cavities of AAO with two different pore sizes (100 and 400 nm) with a fixed the

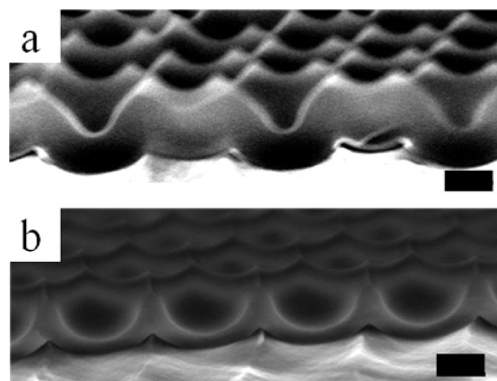


Figure 1. High density array of hemispherical cavities prepared by AAO template: (a) before widening (namely, after two-step anodization) and (b) after widening for 150 min in 0.1 M H₃PO₄ aqueous solution at 30 °C. The scale bar is 200 nm.

center-to-center distance. The pore size was controlled from 100 to 400 nm by increasing pore widening time from 30 to 150 min.

To modify the hydrophilicity of the AAO pore walls, PS-OH, PMMA-OH, and PS-*ran*-PMMA-OH solutions in toluene (1 wt % in solid) were spin-coated on AAO template having hemispherical cavities and annealed at 180 °C for 5 days under vacuum. Nongrafted polymer chains were completely removed by rinsing with toluene. Finally, PS-*b*-PMMA solution in toluene (1 wt %) was spin-coated on the AAO template and annealed at 170 °C for 5 days in vacuum, followed by quenching to room temperature.

Characterization. Transmission electron microscopy (S-7600: Hitachi Ltd.) was performed at an accelerating voltage of 80 kV. To prepare the sample for top-view TEM image, PS-*b*-PMMA samples inside hemispherical cavities were floated onto a 10 wt % hydrofluoric acid solution and transferred to a copper grid with porous carbon film. Then, the samples were stained with ruthenium tetroxide (RuO₄), a selective staining agent for PS.³⁶ To make another sample for cross-sectional TEM image, epoxy resin was dropped on AAO template containing BCPs and heated to 60 °C for 12 h for curing. The aluminum below the AAO template was removed by using CuCl₂ solution (CuCl₂ 9 g, 0.1 M HCl 20 mL, DI water 100 mL). Then, the AAO template was removed by using 0.5 M sodium hydroxide for 90 min, followed by embedding epoxy resin. Ultrathin sections were prepared using a Leica Ultracut Microtome (EM UC6 Leica Ltd.) equipped with diamond knife.³⁷ We also observed, via field emission scanning electron microscopy (FE-SEM; Hitachi S-4800), the arrangement of the PS microdomain inside the hemispherical cavities after the PMMA chains were completely removed by UV irradiation with a maximum intensity at 253.7 nm (Sankyo Denki, G15T8) for 90 min, followed by rinsing with acetic acid, a selective solvent for PMMA, for 90 min and washing with distilled water. To construct a 3D image of TEM (TEM tomography), a projection image at each tilt angle was acquired with a frame size of 1024 × 1024 pixels. A TEM sample holder was scanned over a tilt angle from -60° to +60° in 1°

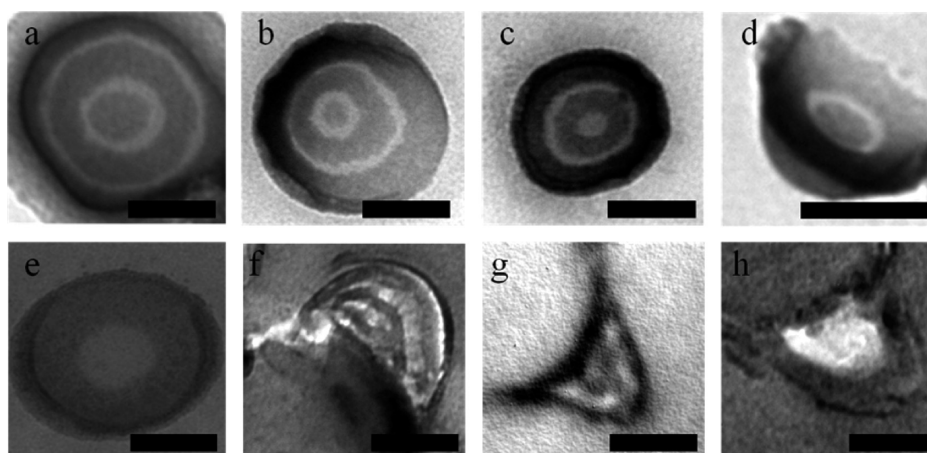


Figure 2. TEM image of PS-*b*-PMMA confined in hemispherical cavities modified by PS-OH brush for different D/L_0 : Top-view TEM images of (a) 4.5, (b) 4.1, (c) 3.1, (d) 2.5, and (e) 1.9. Cross-sectional TEM images corresponding to (b), (c), and (e) are given in (f), (g), and (h), respectively. The scale bar is 100 nm.

increments. Each of the tilt series was aligned separately by using 10 nm gold particles placed on the samples.³⁸

Simulation Methods. The dynamic Metropolis Monte Carlo method with the 8-site bond fluctuation model was used.³⁴ For the simulation of the morphology of symmetric diblock copolymer confined in hemispherical cavities, bead-spring chains of diblock chains, each with $N = 18$ beads consisting of equal number of A and B segments, were generated in a half-spherical volume discretized on lattice. The system was then equilibrated with $\varepsilon = 0.4k_B T$ (corresponding to $\chi N = 20$), where ε and χ are the segmental interaction energy and Flory interaction parameter between A and B, respectively. The surface selectivity of the inner surface in the cavity volume was varied by the areal fraction ϕ of A-segments ($1 - \phi$ of B-segments) covered on the inner surface, whereas the top surface of the cavity volume was modeled to neutral to both blocks. A lattice occupation density was set to be $\phi = 0.5$ for polymer chains in the cavity volume, which corresponds to a molten polymer in the bond fluctuation model. Starting from a random initial configuration, the system was allowed to equilibrate for 5×10^7 Monte Carlo steps (MCS). Configurations were sampled at every 10^4 MCS after equilibration, and the mean local densities of A and B segments were obtained by averaging the densities over 100 samples.

3. RESULTS AND DISCUSSION

Figure 2 shows top-view and cross-sectional TEM images of PS-*b*-PMMA confined in hemispherical cavities modified by the PS brush. Here, the darker phase corresponds to PS microdomains stained with RuO_4 , and the lighter phase to PMMA microdomains. The grafting reaction time of PS-OH brush for all the samples was 5 days at 180 °C, sufficiently long for obtaining equilibrium thickness of the grafted PS chains on the wall. The concentric alternating lamellae are formed regardless of the commensurability condition. This is because the PS microdomains should be always located at the AAO wall by the favorable interaction between PS blocks in PS-*b*-PMMA and grafted PS chains on the wall. The size of the PS microdomains appear bigger than the PMMA microdomains because the PMMA chains were damaged by beam irradiation during TEM experiment, while PS chains stained with RuO_4 were not susceptible to beam damage.^{39,40} The surface tensions of PS and PMMA at the annealing temperature (170 °C) are 29.9 and 29.7 dyn/cm, respectively,⁴¹ indicating that the air surface at the top of confined BCP is nearly neutral to both blocks. At $D/L_0 = 4.5$, five concentric rings with the microdomain sequence of PS/PMMA/PS/PMMA/PS appear,

as shown in Figure 2a. This is consistent with a strong segregation theory which predicts that the number of concentric layers (n) of symmetric block copolymers confined inside spherical cavities whose the inner wall is strongly selective to one of the blocks, is given by $n \cong \lfloor D/L_0 + 0.4 \rfloor + 1$ ($\lfloor x \rfloor$ is the floor function of x).²¹ Although the number of concentric layers is 5 both for $D/L_0 = 4.5$ and 4.1 (Figures 2a and 2b, respectively), the size of the core ring in Figure 2a is larger than that in Figure 2b, indicating that the BCP chains at $D/L_0 = 4.5$ are more stretched. Also, concentric layers with $n = 4$ are clearly seen for $D/L_0 = 3.1$ (Figures 2c and 2g). The concentric ring patterns were also observed even for incommensurability condition, as seen in Figures 2a and 2d, in which the number of the ring is 5 and 3, respectively.

However, when the diameter is nearly twice the bulk domain spacing ($D/L_0 = 1.9$), only two rings are observed instead of the expected three rings (Figures 2e and 2h). We speculated that two main effects are responsible for this rather unexpected result. First, the curvature effect of confining surface plays a certain role for sustaining two-ring structure. It is theoretically predicted for the commensurability behaviors generalized for d -dimensionally confined lamellar microdomains ($d = 1$: film; $d = 2$: cylinder; $d = 3$: sphere) that the curvature of confining surface leads to the shift of D/L_0 value at the transition point of $n \rightarrow n + 1$ toward larger value due to the large bending energy required for concentric layers in curved volume (i.e., the structure with larger n costs a larger bending energy because of the higher curvature of the innermost domain).²¹ For instance, the theory predicts that lamellae confined in spheres undergo $2 \rightarrow 3$ layer-addition transition at $(D/L_0)_{2 \rightarrow 3} = 1.60$, larger than the corresponding value $(D/L_0)_{2 \rightarrow 3} = 1.39$ for lamellae confined between two flat plates.²¹ Second, because the chain ends prefer to locating at the polymer/surface interfaces for entropic reason, the concentric layer in hemispherical cavities with $n = 2$, which can have more chain ends exposed to the air than that with $n = 3$, sustains the stability when compared to BCP confined in fully spherical cavities. It is noted that a large fraction of chain ends for the concentric layers with $n = 3$ (PS-*b*-PMMA/PMMA-*b*-PS/PS-*b*-PMMA/PMMA-*b*-PS configuration across the cavity) should exist at the midspherical surface where PMMA chain ends meet, whereas the concentric layers with $n = 2$ do not have such a midlayer.

To visualize the internal structure of microdomains inside cavities, TEMT experiment was done, and the image is shown in Figure 3. A 3D reconstructed image was obtained from the

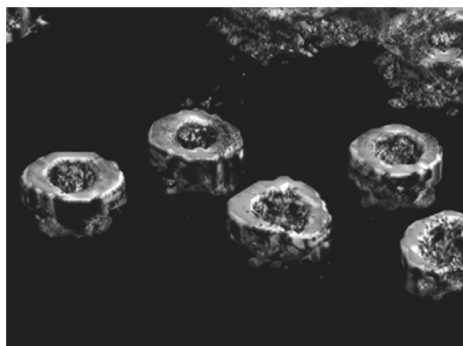


Figure 3. 3D TEMT image of PS-*b*-PMMA confined in hemispherical cavities modified by PS-OH brush for $D/L_0 = 1.9$. Here, only PS microdomains are shown.

2D projection image of Figure 2e. Since bright PMMA appears transparent for 3D visualization, only the PS block is seen in the TEMT image, clearly showing a cup-like structure of the PS microdomain.

Figure 4 gives the microdomain arrangement inside the hemispherical cavities modified by PS-*ran*-PMMA brushes. For

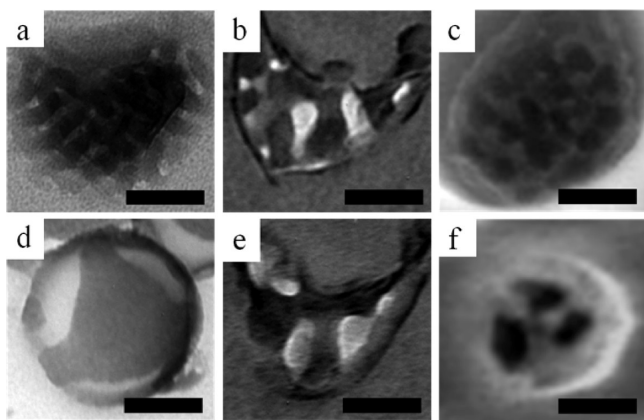


Figure 4. Top-view (a, d), cross-sectional TEM images (b, e), and FE-SEM images (c, f) of PS-*b*-PMMA confined inside the hemispherical cavities modified by PS-*ran*-PMMA-OH brush for two values of D/L_0 : 4.5 (top panel) and 2.0 (bottom panel). For FE-SEM images, the PMMA blocks are completely removed by UV irradiation followed by rinsing with acetic acid. The scale bar is 100 nm.

$D/L_0 = 4.5$, concentric rings are not observed, but PS and PMMA lamellae seem to be entangled with each other (top panel images of Figure 4). This might be attributed to the coexistence of lateral and vertical layer orientations. When the confinement becomes stronger (for instance, $D/L_0 = 2.0$), the PS chains are located near the center of the cavity, whereas three half-spherical caps of PMMA chains surround the PS microdomains (bottom panel images of Figure 4). The formation of this interesting morphology could be explained as follows. When the inner surface is neutral to both blocks, the stacking layers consisting of planar slices of hemispherical volume (i.e., half-spherical caps and thumbtack-like layers) are energetically favored compared with entangled PS and PMMA lamellae due to the smaller interfacial area of the former. The

formation of the former structure, however, incurs an entropic penalty associated with nonuniform stretching of BCP chains packed into spherical caps and thumbtack-like layers that have both planar and round surfaces. Obviously, lamellar-like layers are more favored with increasing D/L_0 where nonuniformity in chain stretching is not severe. But, high curvature of hemispherical cavities with smaller D/L_0 prevents the formation of lamellar-like layers, leading to interfacial modulation as seen in Figure 4d. The competing effect associated with interfacial energy and conformational entropy leads to the morphologies shown in Figure 4. Since we found that the selectivity of the brush layer to the PS block in PS-*b*-PMMA significantly changes the microdomain arrangement inside the hemispherical cavities, we changed more systematically the selectivity of the brush layer. Fortunately, this was successfully achieved by changing the reaction times for the grafting PS chains on the cavity walls.

Figure 5a shows the change of the thickness of PS brush layer, measured by spectroscopic ellipsometry, on a neat (and flat) alumina film with grafting time of PS-OH. The change of grafting densities of brush polymers is given in Figure S1b in the Supporting Information. At a 1 h reaction, the brush thickness was ~ 3 nm. With increasing reaction time, the brush layer thickness increases steadily up to ~ 50 h, and then it becomes saturated. With increasing PS brush layer thickness, the contact angle is also increased accordingly, as shown in Figure 5b. Even at 1 h reaction, it increases to 83° from 67° of the neat alumina film. It is noted that the contact angle at 15 min reaction is similar to that modified the PS-*ran*-PMMA brush layer (see the section 2 of the Supporting Information).

Since the contact angle was measured based on flat alumina film, we obtained, via X-ray photoelectron spectroscopy (XPS), the atomic ratio of C/Al on hemispherical cavities as a function of the graft reaction time, and the result is given in Figure 5c. Here, the amount of carbon is directly related to the brush layer of PS. XPS spectra are shown in Figure S2. Comparing Figure 5a (or 5b) with Figure 5c, the change of the ratio of C/Al with grafting time is very similar to that of brush layer thickness (or contact angle) with grafting time. By change of the thickness of PS grafted chains and the contact angle with time, we roughly divided three regions (I, II, and III). The thickness and contact angle of region I are less than 3 nm and 85° , while those of region III are larger than 5 nm and 95° . The microdomain arrangement inside the cavities corresponding to region III was already shown in Figure 2. We found that the microdomain arrangement for region I was comparable to that for neutral brush grafted surface (Figure S3). Thus, we focus on the microdomain arrangement for region II.

Figure 6 shows TEM images of BCPs confined at hemispherical cavities modified by PS-OH brush at five different values of D/L_0 (5.6 to 2.3). PS-OH brush chains were grafted on the cavities wall for a reaction time of 10 h. Although concentric rings are observed, these rings are connected, which is distinctly different from the results given in Figure 2. The formation of the bridge between the rings is due to the existence of concentration fluctuations along the circumferential direction, although the concentration fluctuations along the radial direction become major, which is responsible for the formation of concentric lamellar rings. The former contributes to relieving the chain stretching (or shrinking) formed in the uniform and concentric layers, which gives rise to the circumferential ordering such as bridges. The penalty associated with the increase in the PS/PMMA

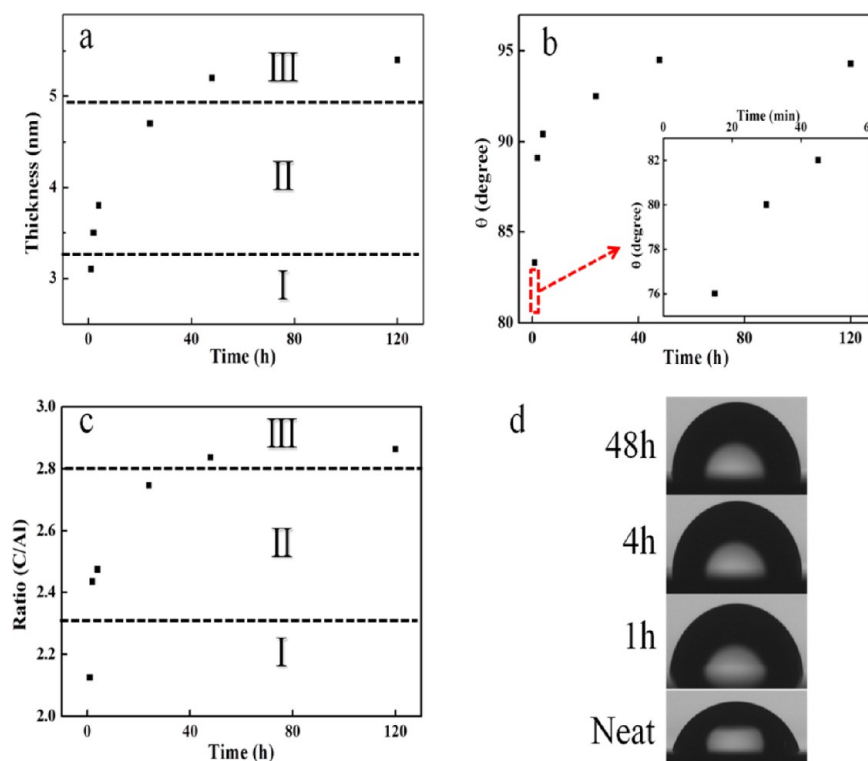


Figure 5. Changes of (a) the graft layer thickness, (b) contact angle (inset: change during short times less than 1 h) on flat AAO film, and (c) the atomic ratio of C/Al with PS-OH grafting time on the wall of hemispherical cavities in AAO. (d) Contact angle images of flat AAO films grafted with PS-OH for various times (0, 1, 4, and 48 h).

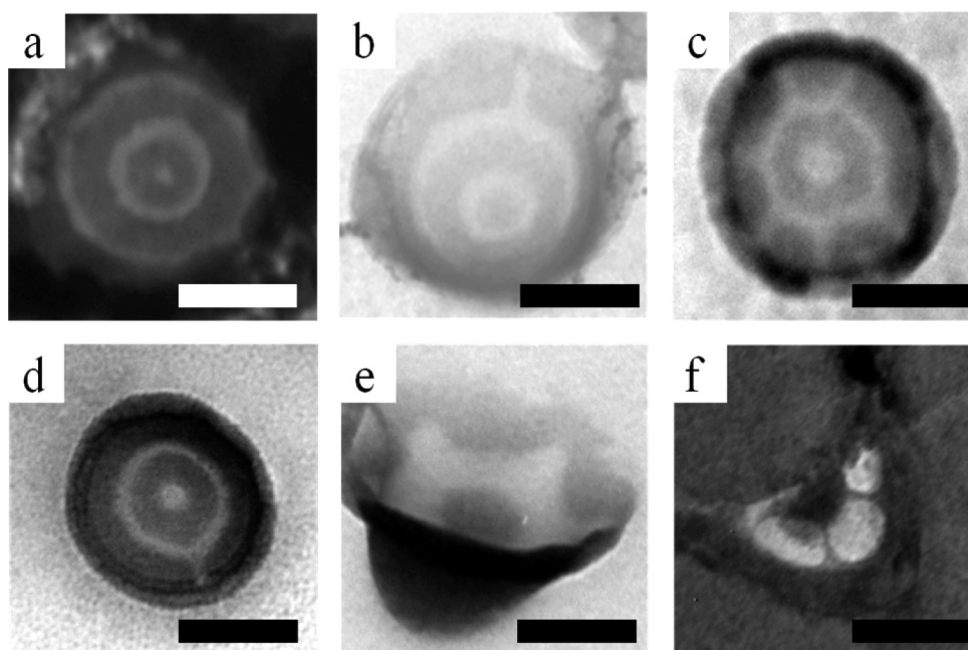


Figure 6. TEM image of PS-*b*-PMMA confined in hemispherical cavities grafted by PS-OH brush for 10 h at five different values of D/L_0 : (a) 5.6, (b) 4.6, (c) 4.1 (d) 3.5, and (e) 2.3. (f) Cross-sectional TEM image corresponding to (e). The scale bar is 100 nm.

interfacial area due to the formation of bridges could be compensated by the reduction of the interfacial energy between BCP chains and the cavity wall where PS chains are loosely grafted. Previously, Yu et al.²⁰ predicted similar layer modulations for lamellae-forming AB diblock confined in 3-D geometry, when the surface selectivity is relatively weak. In this case, the surface-selective, outermost A layer is perforated by

some B chains connecting concentric B layers.²⁰ In the case of strong confinement with $D/L_0 = 2.3$ (Figure 6e), the formation of arc-like interfacial undulation is clearly seen as a result of the lamellar ordering toward the circumferential direction, which could perturb the lamellar ordering along the radial direction. The structural modulation is also confirmed by TEMT experiment. Figure 7 gives 3D TEMT image from 2D

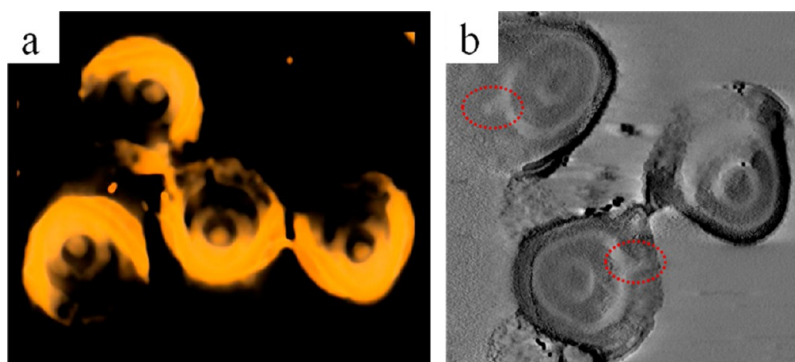


Figure 7. The 3D TEM image of PS-*b*-PMMA confined in hemispherical cavities modified by PS-OH brush for $D/L_0 = 4.6$: (a) captured image of 3D, (b) slice image of (a). Dotted red lines show the bridges. PS-OH brush was grafted on the cavities wall for a grafting time of 10 h.

projection TEM image for $D/L_0 = 4.6$, revealing the bridges from the outermost PMMA layer to the inner surface.

To more systematically investigate the lamellar morphologies confined in the hemispherical cavities as functions of D/L_0 and the surface selectivity, we also obtained confined AB symmetric diblock morphologies by a Metropolis Monte Carlo simulation with a bond fluctuation model. The surface selectivity of the inner surface of hemispherical cavity is controlled by the areal fraction ϕ of A-segments ($1 - \phi$ of B-segments) covered on the inner surface. Figure 8 shows the simulated morphologies as

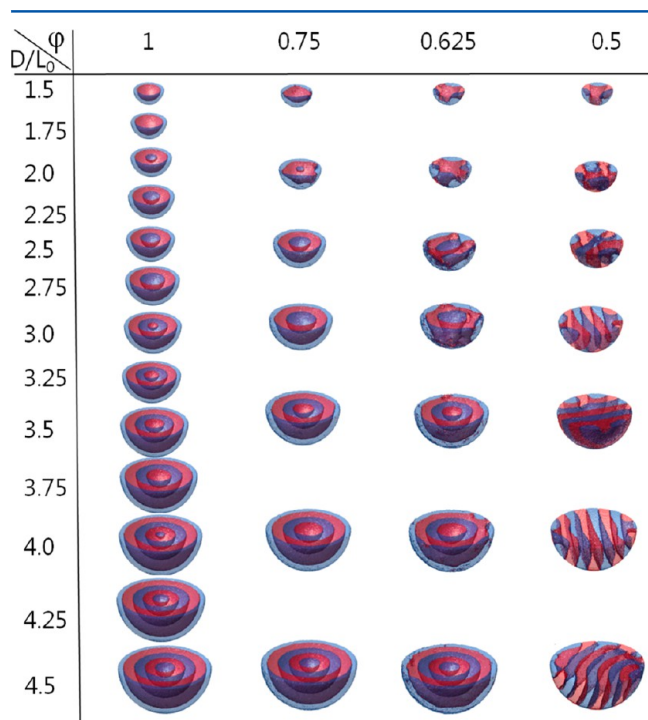


Figure 8. Simulated morphologies as functions of the degree of confinement and the selectivity.

functions of D/L_0 and ϕ . In the case of strongly selective surface ($\phi = 1$), the confined BCP forms perfect concentric layers irrespective of D/L_0 (or commensurability). It is also confirmed from the simulation results that the curvature effect shifts the layer-addition transitions $(D/L_0)_{n \rightarrow n+1}$ toward larger values than that of the flat confinement due to the curvature and chain end effects. The transition point $(D/L_0)_{n \rightarrow n+1}$ from

the simulation result lies between $n - 0.25$ and n , in agreement with the experimental results (Figure 2e).

In the case of weak selective surface ($\phi = 0.75$ and 0.625), undulations of the A/B outermost interface in the concentric layers, often in the form of bridges, are seen in the simulated morphologies. This is more evident as D/L_0 and ϕ decrease. At a relatively weaker confinement where the curvature of concentric layers is small, the interfacial undulation vanishes, which suggests that the interfacial undulation or the bridge formation is attributed to the curvature effect as well as the surface selectivity. When the surface is neutral to both blocks, stacking layers, perpendicular to the top surface, are formed under weaker confinement ($D/L_0 > 3.0$), whereas the stronger confinement modulates the A/B interface resulting from two counter effects of uniform stretching against minimizing A/B interfacial area due to high curvature imposed by the confinement.

Shi and Li²² showed that when block copolymers are confined inside fully spherical cavities, strongly selective surfaces lead to lamellae parallel to the surfaces, whereas neutral surfaces lead to lamellae perpendicular to the surfaces. Our experiment and simulation results also show that the lamellar-forming microdomains are transformed from concentric lamellae to standing lamellae when the cavity surfaces are changed from strongly selective to neutral. Thus, the surface selectivity effect on alignment of block copolymer microdomains confined inside hemispherical cavity is similar to that confined inside fully spherical cavity.

In conclusion, the morphological structures of symmetric PS-*b*-PMMA BCPs confined in the hemispherical pores were investigated by varying the surface selectivity of the inner surface of the cavities. When the inner surface is selective to one of the blocks, concentric layers or their circumferentially modulated structures such as bridges or interfacial undulation are found by changing the cavity diameter. On the other hand, when the surface is neutral to both blocks, stacking lamellar layers or partially stacking layers are found. The experimentally observed morphological structures in hemispherical cavities agree with Monte Carlo-simulated structures.

■ ASSOCIATED CONTENT

📄 Supporting Information

Preparation of hemispherical cavities, characterization of brush layers grafted on the cavity wall, and hemispherical cavities modified by PMMA-OH. This material is available free of charge via the Internet at <http://pubs.acs.org>.

■ AUTHOR INFORMATION

Corresponding Author

*E-mail: jkkim@postech.ac.kr (J.K.K.), junehuh@yonsei.ac.kr (J.H.).

Notes

The authors declare no competing financial interest.

■ ACKNOWLEDGMENTS

This work was supported by the National Creative Research Initiative Program of the National Research Foundation of Korea of the Ministry of Education, Science and Technology, Korea. Small-angle X-ray scattering was performed at PAL beamline (4C1) supported by POSCO and NRF.

■ REFERENCES

- (1) Bates, F. S. *Science* **1991**, *251*, 898–905.
- (2) Kim, J. K.; Lee, J. I.; Lee, D. H. *Macromol. Res.* **2008**, *16*, 267–292.
- (3) Kim, J. K.; Yang, S. Y.; Lee, Y.; Kim, Y. *Prog. Polym. Sci.* **2010**, *35*, 1325–1349.
- (4) Jo, A.; Joo, W.; Jin, W. H.; Nam, H.; Kim, J. K. *Nat. Nanotechnol.* **2009**, *4*, 727–731.
- (5) Kang, Y. J.; Walish, J. J.; Gorishnyy, T.; Thomas, E. L. *Nat. Mater.* **2007**, *6*, 957–960.
- (6) Yang, S. Y.; Ryu, I.; Kim, H. Y.; Kim, J. K.; Jang, S. K.; Russell, T. P. *Adv. Mater.* **2006**, *18*, 709–712.
- (7) Yang, S. Y.; Park, J.; Yoon, J.; Ree, M.; Jang, S. K.; Kim, J. K. *Adv. Funct. Mater.* **2008**, *18*, 1371–1377.
- (8) Lee, J. I.; Cho, S. H.; Park, S.-M.; Kim, J. K.; Kim, J. K.; Yu, J.-W.; Kim, Y. C.; Russell, T. P. *Nano Lett.* **2008**, *8*, 2315–2320.
- (9) Yang, S. Y.; Yang, J.-A.; Kim, E. S.; Jeon, G.; Oh, E. J.; Choi, K. Y.; Hahn, S. K.; Kim, J. K. *ACS Nano* **2010**, *4*, 3817–3822.
- (10) Cho, W. J.; Kim, Y.; Kim, J. K. *ACS Nano* **2012**, *6*, 249–255.
- (11) Han, S. H.; Pryamitsyn, V.; Bae, D. S.; Kwak, J. H.; Ganesan, V.; Kim, J. K. *ACS Nano* **2012**, *6*, 7966–7972.
- (12) Albrecht, T. T.; Schotter, J.; Kästle, G. A.; Emley, N.; Shibauchi, T.; Elbaum, L. K.; Guarini, K.; Black, C. T.; Tuominen, M. T.; Russell, T. P. *Science* **2000**, *290*, 2126–2129.
- (13) Doerk, G. S.; Liu, C.-C.; Cheng, J. Y.; Renttner, C. T.; Pitera, J. W.; Krupp, L. E.; Topuria, T.; Arellano, N.; Sanders, D. P. *ACS Nano* **2013**, *7*, 276–285.
- (14) Ma, M.; Krikorian, V.; Yu, J. H.; Thomas, E. L.; Rutledge, G. C. *Nano Lett.* **2006**, *6*, 2969–2972.
- (15) Kim, T. H.; Hwang, J.; Hwang, W. S.; Huh, J.; Kim, H.-C.; Kim, S. H.; Hong, J. M.; Thomas, E. L.; Park, C. *Adv. Mater.* **2008**, *20*, 522–527.
- (16) Shin, K.; Xiang, H.; Moon, S. I.; Kim, T.; McCarthy, T. J.; Russell, T. P. *Science* **2004**, *306*, 76.
- (17) Jeon, S.; Yi, G.; Yang, S. *Adv. Mater.* **2008**, *20*, 1–6.
- (18) Higuchi, T.; Tajima, A.; Motoyoshi, K.; Yabu, H.; Shimomura, M. *Angew. Chem., Int. Ed.* **2008**, *120*, 8164–8166.
- (19) Yu, B.; Sun, P.; Chen, T.; Jin, Q.; Ding, D.; Li, B.; Shi, A. C. *Phys. Rev. Lett.* **2006**, *96*, 138306.
- (20) Li, W.; Wickham, R. A. *Macromolecules* **2006**, *39*, 8492–8498.
- (21) Yu, Bin.; Li, B.; Jin, Q.; Ding, D.; Shi, A. C. *Macromolecules* **2007**, *40*, 9133–9142.
- (22) Huh, J.; Park, C.; Kwon, Y. K. *J. Chem. Phys.* **2010**, *133*, 114903.
- (23) Shi, A. C.; Li, B. *Soft Matter* **2013**, *9*, 1398–1413.
- (24) Lambooy, P.; Russell, T. P.; Kellogg, G. J.; Mayes, A. M.; Gallagher, P. D.; Satija, S. K. *Phys. Rev. Lett.* **1994**, *72*, 2899–2902.
- (25) Jeon, S. J.; Yi, G. R.; Koo, C. M.; Yang, S. M. *Macromolecules* **2007**, *40*, 8430–8439.
- (26) Higuchi, T.; Tajima, A.; Motoyoshi, K.; Yabu, H.; Shimomura, M. *Angew. Chem., Int. Ed.* **2009**, *48*, 5125–5128.
- (27) Arsenault, A. C.; Rider, D. A.; Tetreault, N.; Chen, J. I.; Coombs, N.; Ozin, G. A.; Manners, I. *J. Am. Chem. Soc.* **2005**, *127*, 9954–9955.
- (28) Li, L.; Matsunaga, K.; Zhu, J.; Higuchi, T.; Yabu, H.; Shimomura, M.; Jinnai, H.; Hayward, R. C.; Russell, T. P. *Macromolecules* **2010**, *43*, 7807–7812.
- (29) Yabu, H.; Jinno, T.; Koike, K.; Higuchi, T.; Shimomura, M. *Macromolecules* **2011**, *44*, 5868–5873.
- (30) Higuchi, T.; Motoyoshi, K.; Sugimori, H.; Jinnai, H.; Yabu, H.; Shimomura, M. *Soft Matter* **2012**, *8*, 3791–3797.
- (31) Bae, D.; Cho, W. J.; Jeon, G.; Byun, J.; Kim, J. K. *J. Phys. Chem. C* **2012**, *116*, 26523–26528.
- (32) Jeong, S.-J.; Kim, J. E.; Moon, H.-S.; Kim, B. H.; Kim, S. M.; Kim, J. B.; Kim, S. O. *Nano Lett.* **2009**, *9*, 2300–2305.
- (33) Li, A. P.; Muller, F.; Birner, A.; Nielsch, K.; Gosele, U. *Adv. Mater.* **1999**, *11*, 483–487.
- (34) Yu, J.; Geng, C.; Zeng, Y.; Yan, Q.; Wang, X.; Shen, D. *ACS Macro Lett.* **2012**, *1*, 62–66.
- (35) Kim, S. H.; Jo, W. H.; Kim, J. *Macromolecules* **1996**, *29*, 6933–6940.
- (36) Bolze, J.; Kim, J.; Huang, J.; Rah, S.; Youn, H. S.; Lee, B.; Shin, T. J.; Ree, M. *Macromol. Res.* **2002**, *10*, 2.
- (37) Trent, J. S.; Scheinbeim, J. I.; Couchman, P. R. *Macromolecules* **1983**, *16*, 589–598.
- (38) Lipomi, D. J.; Martinez, R. V.; Whitesides, G. M. *Angew. Chem., Int. Ed.* **2011**, *50*, 2–20.
- (39) Jinnai, H.; Spontak, R. J.; Nishi, T. *Macromolecules* **2010**, *43*, 1675–1688.
- (40) Carvalho, B. L.; Thomas, E. L. *Phys. Rev. Lett.* **1994**, *73*, 3321–3324.
- (41) Sohn, B. H.; Yun, S. H. *Polymer* **2002**, *43*, 2507–2512.
- (42) Wu, S. J. *Phys. Chem.* **1970**, *74*, 632–638.